Construction and Building Materials 250 (2020) 118867

Contents lists available at ScienceDirect

Construction and Building Materials

journal homepage: www.elsevier.com/locate/conbuildmat

Numerical investigation on ballistic performance of coarse-aggregated layered UHPFRC

Y.Y.Y. Cao [a], Qingliang Yu [a,b,*], W.H. Tang [c], H.J.H. Brouwers [a]

[a] Department of the Built Environment, Eindhoven University of Technology, P.O. Box 513, 5600 MB Eindhoven, the Netherlands
[b] School of Civil Engineering, Wuhan University, 430072 Wuhan, PR China
[c] College of Liberal Arts and Science, National University of Defense Technology, 410073 Changsha, PR China

HIGHLIGHTS

- The dynamic response of UHPFRC is modelled by HJC constitutive model in LS-DYNA.
- The numerical simulation results coincide very well with the experimental results.
- The layer interface affects the pressure distribution in the triple-layered UHPFRC.
- The DOP decreases with the target thickness; and critical thickness is derived.
- The h_e increases with the bullet velocity, and layered structure shows the reduced h_e.

ARTICLE INFO

Article history:
Received 31 January 2020
Received in revised form 5 March 2020
Accepted 22 March 2020

Keywords:
Ultra-High Performance Fiber Reinforced Concrete (UHPFRC)
Penetration resistance
Coarse aggregate
Layered structure
LS-DYNA

ABSTRACT

The impact resistance of coarse-aggregated layered Ultra-High Performance Fiber Reinforced Concrete (UHPFRC) is investigated numerically with LS-DYNA. The Holmquist Johnson Concrete (HJC) model is employed to describe the dynamic behavior of the UHPFRC, and the effect of the coarse aggregates is reflected in the pressure-compaction relation. Mechanical tests are conducted to obtain the material-related inputs for the numerical model, and ballistic experiments are applied to calibrate the model parameter as well as to validate the simulation results. After valuation, the ballistic histories of the projectile and the penetration processes in the UHPFRC targets are analyzed. Furthermore, the study discusses the effects of the target thickness on the depth of penetration, showing the possibility to replace a thicker single-layered target by a thinner triple-layered one to achieve the same level of protection. Finally, perforation limits of the single- and tripled-layered UHPFRC at different impact velocities are estimated, based on which the ACE formulae are modified to accurately predict the perforation limit of the coarse-aggregated layered UHPFRC. The numerical simulations in this study reveal that the triple-layered target requires fewer dosages of cement and steel fibers in comparison to its single-layered counterpart with the same level of ballistic protection.

1. Introduction

The increasing risks of terrorist attacks in the current world clearly show the necessity of improving the impact resistance of important buildings and infrastructures. The advanced mechanical properties [1–3] make Ultra-High Performance Fiber Reinforced Concrete (UHPFRC) a promising candidate for these infrastructures. The superior resistance of UHPFRC has been revealed in literature. For instance, the impact responses of UHPFRC against deformable and non-deformable projectiles were evaluated by Máca et al. [4]; the significantly improved resistance of UHPFRC was confirmed in their study and an optimal fiber volume fraction of 2% was obtained. Liu et al. [5] analyzed experimentally and numerically the ballistic resistance of UHPFRC, the results of which presented that UHPFRC has advantages regarding the depth of penetration (DOP), crater diameter and volume loss. Yu et al. [6] investigated the ballistic performances of UHPFRC against 7.62 mm projectile at 830 m/s, and claimed that the UHPFRC containing hybrid fibers is more efficient than that with only the hooked-end fiber.

Generally, conventional UHPFRC, e.g. those mentioned above, only utilizes fine particles [7,8]. On the one hand, using only fine

* Corresponding author at: Department of the Built Environment, Eindhoven University of Technology, P.O. Box 513, 5600 MB Eindhoven, the Netherlands.
E-mail address: q.yu@bwk.tue.nl (Q. Yu).

https://doi.org/10.1016/j.conbuildmat.2020.118867
0950-0618/

aggregates in UHPFRC can promote its strength enhancement, thus benefiting the reduction of DOP [9]. On the other hand, the advantages of coarse aggregates on enhancing its impact resistance, e.g. eroding the projectile and deviating the ballistic trajectory, are consequently sacrificed [10,11]. Only a few studies are available concerning the penetration resistance of coarse-aggregated UHPFRC, and positive results are obtained in these studies, showing that the coarse aggregates are beneficial to reduce both the DOP and the area of damage [12–14]. Nevertheless, the compressive strength $\sigma_{c,s}$ of these coarse-aggregated UHPFRC are relatively low, e.g. the 28-day $\sigma_{c,s}$ of the UHPFRC with coarse basalt aggregates are around 106 MPa [12] and 119 MPa [14], and the 160-day $\sigma_{c,s}$ in [13] is about 128 MPa. That being the case, the coarse-aggregated UHPFRC in these studies actually fail to meet the strength requirement of UHPFRC, i.e. having a compressive strength of at least 150 MPa at 28 days [15].

In addition to taking the advantages of coarse aggregates, another innovative approach to improve the impact resistance of UHPFRC may be applying the concept of layered-structure. Our previous study concerning static bending of UHPFRC [16] exhibited that the double-layered UHPFRC has an enhanced energy absorption capacity over its single-layered counterpart. It was revealed that the layer interface in the double-layered UHPFRC facilitated the initiation of multiple micro-cracks, promoting the energy dissipation of the specimen [16]. With regard to the ballistic impact, Quek et al. [17] claimed that the four-layered concrete target ($\sigma_{c,s} \leq 110$ MPa) developed in their study achieved a superior ballistic resistance, and that the layer delamination benefited the consumption of the projectile's kinetic energy. Nonetheless, the subject of their study is high-strength concrete instead of UHPFRC, and the effects of the layer interface on the penetration process are not addressed.

The above findings inspired us to design coarse-aggregated layered UHPFRC to achieve an excellent ballistic resistance. Understanding the dynamic performances of this coarse-aggregated layered UHPFRC is therefore a significant issue. Ballistic experiments can provide direct results; however, the expensive test facilities and the time-consuming test process put limits on conducting massive experiments in this field [18,19]. Empirical and theoretical formulae [20] can predict some important ballistic responses, e.g. the DOP, perforation limit and residual velocity; nevertheless, these formulae cannot reproduce the dynamic stress and damage distributions in the impacted concrete. On the other hand, with the advancement of computer technology, numerical simulations of concrete against ballistic impacts become feasible. A number of commercial software, such as LS-DYNA, ABAQUS and AUTODYN, can be utilized to model the response of concrete subjected to ballistic impacts, providing valuable information on the real-time interaction between the projectile and the concrete.

Modelling the dynamic response of UHPFRC under penetration is challenging [19]. As a result of the rate effect, the behavior of UHPFRC subjected to dynamic loads is more complicated in comparison to that under static load [1]. Moreover, UHPFRC is practically idealized as a homogeneous material in macroscale simulations. However, concrete is actually inhomogeneous and has multiple phases (e.g. matrix, aggregates and steel fibers), which makes modelling the constitutive relation of the "homogenized" UHPFRC rather difficult [21]. As a consequence, choosing the appropriate material models and determining the suitable parameters to reflect the influences of important UHPFRC components, e.g. the coarse aggregate, under dynamic loads are of great significance for the success of these macroscale simulations. Peng et al. [22] modelled the ballistic behaviors of concrete target at both macroscale and mesoscale (with coarse aggregates explicitly presented). Comparing the relative DOP in their simulations exhibits that the macroscale model can give results close to that from the mesoscale model as long as appropriate material models were applied, especially for the cases where the ratio between the aggregate size and the projectile diameter is smaller than 2. This confirms the possibility of applying homogenous models to simulate the ballistic performance of concrete at macroscale.

As with UHPFRC, several studies have been conducted to simulate its ballistic response at macroscale. For example, Liu et al. [19] applied the K&C model in LS-DYNA to investigate the effects of UHPFRC compressive strength, projectile velocity and nose shape on the DOP and the cratering damage size. Yu [23] used the HJC model to describe the ballistic response of UHPFRC by LS-DYNA, and it was claimed that the obtained numerical simulations agreed well with the experimental results. Sovják et al. [24] numerically evaluated the resistance of slim UHPFRC panels with the RHT model in AUTODYN, and the effect of fibers was incorporated in the model by increasing its fracture energy. It is noteworthy that the above numerical studies only focus on conventional UHPFRC with a single-layer and fine particles, i.e. the influences of the layered structure and the coarse aggregates are not addressed.

This study investigates numerically the ballistic performances of coarse-aggregated layered UHPFRC at macroscale. LS-DYNA is employed to execute the simulations, and the effect of the coarse aggregates is reflected by the crushing pressure in the HJC model. After validating the model against experiments, the dynamic penetration processes inside the coarse-aggregated layered UHPFRC are analyzed. Moreover, influences of the target thickness on the DOP are discussed, and the perforation limits of the single- and tripled-layered UHPFRC at different penetration velocities are evaluated. The study confirms the advantages of the coarse-aggregated layered UHPFRC and advances the understanding of its ballistic performances.

2. Mechanical and ballistic experiments

Mechanical and ballistic experiments of the coarse-aggregated layered UHPFRC are conducted to provide inputs for the numerical model, as well as to validate the simulations.

2.1. Materials and mix design

The recipes of the coarse-aggregated UHPFRC are given in Table 1, including Portland Cement I 52.5R (HeidelbergCement Benelux), limestone powder (CB2M), micro-silica (Elkem Grade 920E D), sand (DIN EN 196-1), basalt aggregates of four size groups, water, and a PCE based superplasticizer (solid content of 35%). The straight steel fiber (Dramix OL 13/0.20) is used, which has a length of 13 mm and diameter of 0.2 mm. The density of the fiber is around 7850 kg/m^3.

The fractions of the basalt aggregates are calculated by the Brouwers mix design method [25–27] to achieve an optimal packing density of the mixture:

Table 1
Recipes of the UHPFRC (kg/m^3).

Identification	U8*a*	U8*a*1*s*	U16*a*1*s*
Portland Cement CEM I 52.5R	588.0	588.0	525.0
Limestone powder	156.8	156.8	140.0
Micro-silica	39.2	39.2	35.0
Sand	839.9	839.9	699.3
Basalt aggregate (size 2–5 mm)	413.2	413.2	445.2
Basalt aggregate (size 5–8 mm)	232.3	232.3	186.9
Basalt aggregate (size 8–11 mm)	0	0	147.8
Basalt aggregate (size 8–16 mm)	0	0	209.6
Water	149.0	157.0	161.0
Superplasticizer	9.4	8.5	4.5
Straight steel fiber (%)	0	1.0	1.0

$$P_t(D) = \frac{D^q - D^q_{min}}{D^q_{max} - D^q_{min}} \quad (1)$$

$$R^2 = 1 - \frac{\sum_{i=1}^{n} [P_m(D_i) - P_t(D_i)]^2}{\sum_{i=1}^{n} \left[P_m(D_i) - \frac{1}{n}\sum_{i=1}^{n} P_m(D_i)\right]^2} \quad (2)$$

where q is the distribution modulus, and the value of 0.22 is applied for UHPFRC [23]. D is the particle size; D_{min} and D_{max} are the minimum and maximum values, respectively. $P_m(D)$ is the cumulative fraction of the total solid with a size smaller than D, and $P_t(D)$ presents the targeted cumulative fraction.

An optimization algorithm is applied to achieve an optimal fit between $P_m(D)$ and $P_t(D)$, i.e. a maximum R^2 (the quality of fit between the designed and the target distributions). Examples of the particle size distribution curves of the designed coarse-aggregated UHPFRC mixture are shown in Fig. 1 [28]. More information about the detailed properties of the applied ingredients can be found in [28,29].

2.2. UHPFRC targets

The coarse-aggregated UHPFRC with single and triple layers were tested, as shown in Table 2. The thickness of the UHPFRC target is 90 mm and the diameter is about 275 mm. U in the identifications represents UHPFRC. The identification of the third is divided by dashes, showing that it is a layered target. The layer thickness is given in the brackets (in mm). The numbers before *a* and *s* are the maximum aggregate size (in mm) and the fiber volume fraction, respectively. For instance, U16*a*1*s*(30)-8*a*1*s*(30)-16*a*1*s*(30) is a triple-layered UHPFRC target with an equal layer thickness of 30 mm; the maximum aggregate sizes of the three layers are 16 mm, 8 mm and 16 mm, respectively; and 1% (volume fraction) of the steel fibers are incorporated in each of the three layers (see Table 2). As can be noticed, the larger aggregates are arranged in the two outer layers of the triple-layered UHPFRC target. This aggregate size arrangement is determined based on: (1) the more severe damage of the front and rear surfaces of the target compared to its middle region [23,30], and (2) the contribution of the larger aggregates to decreasing the damage size [12–14]. A reverse order of the layers, e.g. U8*a*1*s*(30)-16*a*1*s*(30)-8*a*1*s*(30), is expected to result in an inferior impact resistance due to the less efficient effect of the 8 mm aggregates on reducing the damage of the two outer surfaces.

2.3. Sample preparation and testing

The mixing of the UHPFRC mixture was conducted at room temperature, and the procedure is illustrated in Fig. 2.

Cylindrical moulds were utilized to cast the UHPFRC targets. For the triple-layered UHPFRC, the layers were cast subsequently after a short time interval of 45 min [16]. The UHPFRC samples were demolded 24 h after casting and they were cured in water at room temperature of 20 ± 1 ℃. The ballistic tests were conducted at 56 days with in-service 7.62 mm × 51 AP projectile. The impact velocity V_0 was around 840 m/s. The test setup is shown in Fig. 3. A specially designed fixing frame was used to hold the cylindrical UHPFRC target, and a white board was put behind the frame to check the trace of the projectile in the case of ballistic perforation. The targets were cut to measure the DOP after the ballistic tests [31].

Additionally, 100 mm UHPFRC cubes were prepared to test the compressive, splitting tensile and bond strengths of the designed

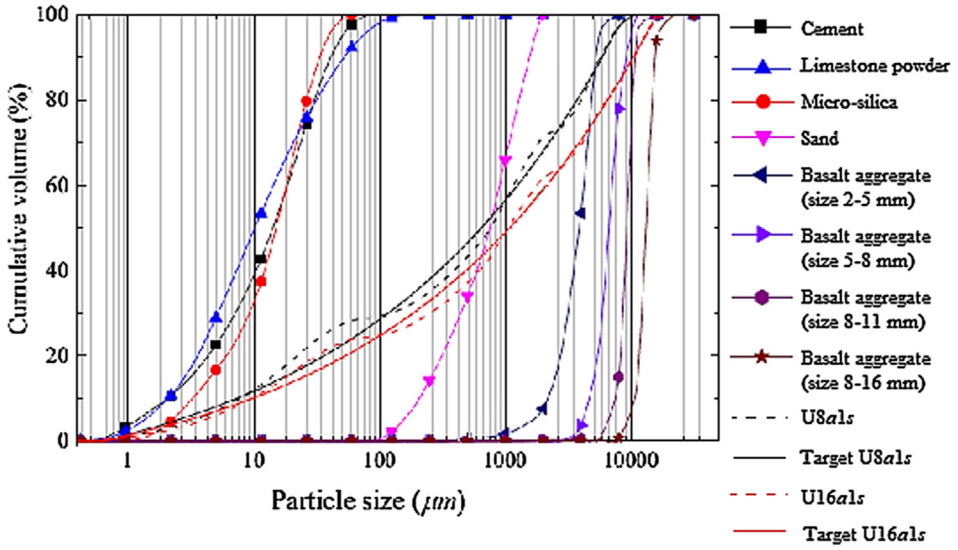

Fig. 1. Particle size distribution curves [28].

Table 2
Single- and triple-layered UHPFRC.

Identification	Layer thickness			Maximum aggregate size			Fibre volume fraction		
	mm			mm			%		
	1st layer	2nd layer	3rd layer	1st layer	2nd layer	3rd layer	1st layer	2nd layer	3rd layer
U8*a*1*s*(90)	90	–	–	8	–	–	1	–	–
U16*a*1*s*(90)	90	–	–	16	–	–	1	–	–
U16*a*1*s*(30)-8*a*1*s*(30)-16*a*1*s*(30)	30	30	30	16	8	16	1	1	1

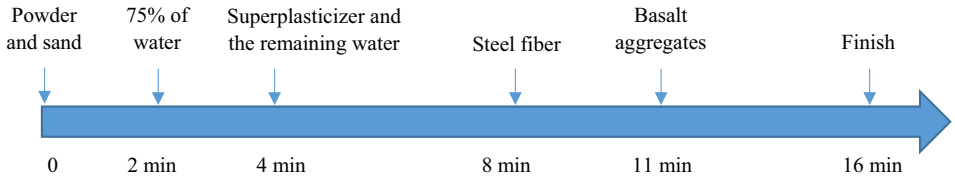

Fig. 2. Illustration of mixing procedure.

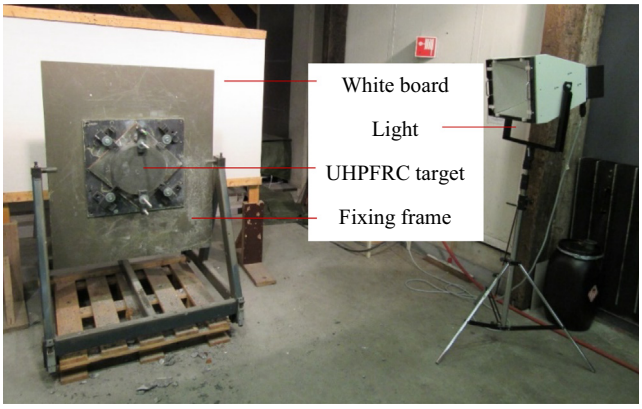

Fig. 3. Fixing frame in the ballistic test.

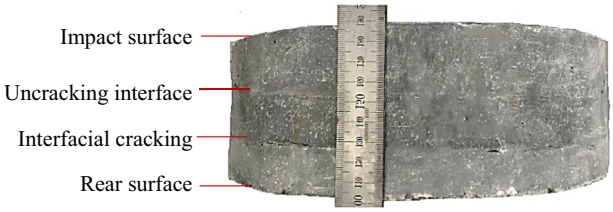

Fig. 4. Interfacial cracking in U16*a*1*s*(30)-8*a*1*s*(30)-16*a*1*s*(30).

UHPFRC at 56 days. A universal testing machine (DIGIMAXX C-20, maximum load capacity of 4000 kN) was utilized for the mechanical experiments. The compressive and splitting tensile strengths of the UHPFRC were tested according to EN 12390-3 [32] and EN 12390-6 [33], respectively. The interface bond strength was tested applying the splitting method [34].

2.4. Experimental results

2.4.1. Compressive, tensile and bonding strengths

Thanks to the optimized mix design, the coarse-aggregated UHPFRC developed in this study shows satisfying mechanical properties, complying with the strength requirements of UHPFRC. The compressive strengths of U8*a*, U8*a*1*s* and U16*a*1*s* mixtures are around 150 MPa, 158 MPa and 161 MPa; while the corresponding splitting tensile strengths are 7.2 MPa, 12.3 MPa and 14.6 MPa, respectively. The bond strength between the U8*a*1*s* and U16*a*1*s* layers is about 7.0 MPa.

2.4.2. Penetration test results

The DOP and the crater size D_{eq} of the single- and triple-layered UHPFRC targets are given in Table 3. D_{eq} was calculated as $D_{eq} = \sqrt{D_1 D_2}$, where D_1 and D_2 are the crater size measured at two perpendicular directions. With regard to the single-layered UHPFRC, increasing the maximum aggregate size from 8 mm to 16 mm increases the ballistic resistance. This enhanced resistance is because that the higher strength and hardness of the coarse aggregates contribute to consuming more kinematic energy of the projectile, which reduces its penetration velocity [10,12,22]. Moreover, comparing U16*a*1*s*(30)-8*a*1*s*(30)-16*a*1*s*(30) and U8*a*1*s*(90) in Table 3 presents that applying a layered structure can further reduce the DOP. As expected, discontinuous cracks are observed along the layer interface, as shown in Fig. 4. This interfacial cracking can further facilitate the energy dissipation of the projectile [17], leading to the reduced DOP in the triple-layered target.

Table 3
Penetration test results of designed UHPFRC.

Identification	V_0 (m/s)	DOP (mm)	D_{eq} (mm)
U8*a*1*s*(90)	841.9	60.0	70.0
U16*a*1*s*(90)	840.7	55.0	63.0
U16*a*1*s*(30)-8*a*1*s*(30)-16*a*1*s*(30)	839.3	52.5	67.9

3. Numerical modelling

3.1. Overview of the model

Three dimensional models of the UHPFRC targets and the projectile are built in LS-DYNA, as shown in Fig. 5. In order to improve the computational efficiency, only one quarter of the test arrangement is modelled. Symmetric boundary conditions are imposed on models and fixed boundary conditions are imposed on the back edge of the targets. The penetration process is simulated based on the explicit time integration. To achieve the stability of the solution, a scale factor of 0.67 for the computed time step is applied [36].

3D solid 164 element is used in the simulation. As shown in Fig. 5, the target is divided into 45 indices in the direction of penetration and 30 indices along its radius direction. The length of the element gradually increases along the target radius, and it is finer in the region where the projectile contacts the concrete. The minimum element sizes of the target and the projectile are comparable, i.e. about 1.2 mm and 1 mm, respectively. The results of mesh convergence study are presented in Fig. 6, in which the minimum mesh size of the target changes from 1.2 to 2.0 mm. The figure shows that 1.2 mm is sufficiently fine and the mesh is therefore adopted in the simulations. For the triple-layered target U16a1s (30)-8a1s(30)-16a1s(30), a thin layer of interfacial elements (with a thickness of 0.5 mm) is added in between the U16a1s layers and the U8a1s layer, and the interface elements have shared nodes with the elements of the U8a1s and U16a1s layers. In other words, there is no direct contact between the U8a1s and U16a1s layers, and their connection is considered by the thin interfacial layer fixed to the target layers.

3.2. Material models

3.2.1. Projectile

The penetration velocities in the experiments are around 840 m/s, which fall within the range of non-deformable (rigid) penetration ($V_0 \leq 1000$ m/s) [19]. Furthermore, the hard core of

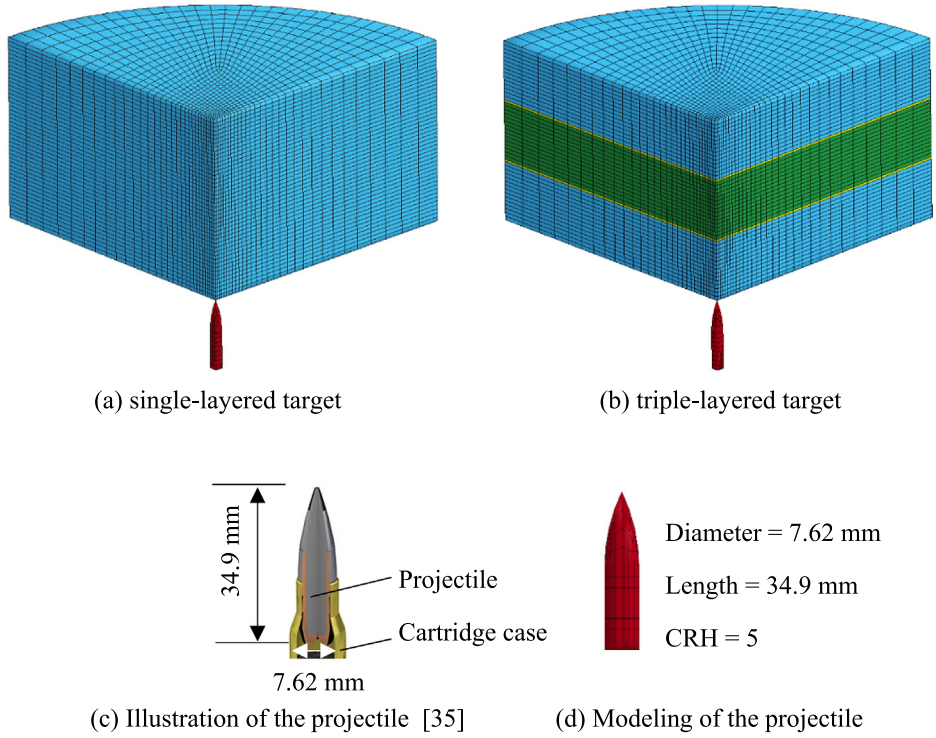

Fig. 5. Models of the penetration test. (See above-mentioned references for further information.)

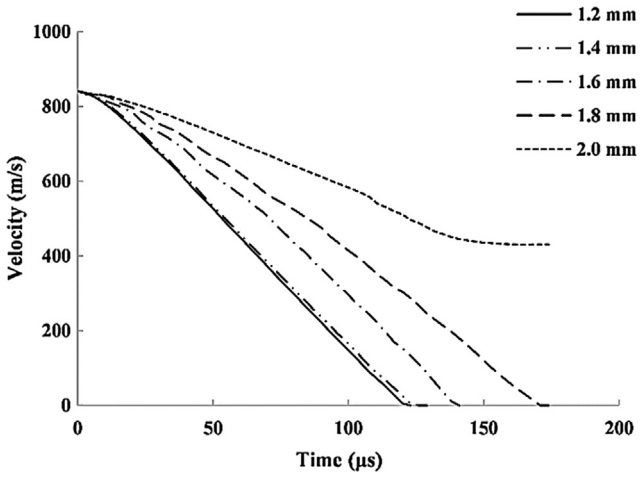

Fig. 6. Mesh convergence study.

the projectile after the ballistic test is compared to that before the test. Despite the slight scratches on the surface, the main body of the hard core after the ballistic test has very limited deformation thanks to the stiff material of the hard core and its small size. Therefore, the deformation of the projectile is neglected in this simulation, and it is modeled as a rigid body using the material model *MAT_RIGID (MAT_020) in LS-DYNA. The input parameters for the projectile are listed in Table 4. The contact between the projectile and UHPFRC is modelled with "CONTACT_ERODING_SURFACE_TO_SURFACE".

3.2.2. UHPFRC target

The HJC constitutive model *MAT_JOHNSON_HOLMQUIST_CONCRETE (MAT_111) is adopted for the UHPFRC and the layer interface. This model is suitable to describe the response of cementitious materials subjected to high strain rates, large deformations, and high hydrostatic pressures [37,38], and it has been widely employed to model the ballistic performance of concrete [22,23].

Table 4
Rigid model inputs for the projectile.

Parameters	Projectile
Density ρ (kg/m^3)	7850
Young's modulus E (GPa)	206
Poisson's ratio	0.3

In the HJC model, the yield surface is [37]:

$$\sigma^* = \left[A_c(1-D_c) + B_c P^{*N_c}\right](1 - C_c \ln \dot{\varepsilon}^*) \quad (3)$$

where σ^* is the normalized equivalent stress, P^* is the normalized pressure.$\dot{\varepsilon}^* = \dot{\varepsilon}/\dot{\varepsilon}_0$ is the dimensionless strain rate ($\dot{\varepsilon}$ and $\dot{\varepsilon}_0$ = 1.0 s^{-1} are the actual and reference stain rates, respectively). A_c, B_c, C_c and N_c are input parameters.

The damage D is accumulated as a function of the equivalent plastic strain ε_p, plastic volumetric strain μ_p, and the total plastic strain until fracture $\varepsilon_p^f + \mu_p^f$ [39]:

$$D = \sum \frac{\Delta\varepsilon_p + \Delta\mu_p}{\varepsilon_p{}^f + \mu_p{}^f} \quad (4)$$

$$\varepsilon_p{}^f + \mu_p{}^f = D_1(P^* + T^*)^{D_2} \geqslant EFMIN \quad (5)$$

where D_1 and D_2 are the damage parameters. $T^* = T/\sigma_{c,s}$ is the normalized maximum tensile hydrostatic pressure and T is the maximum tensile pressure. *EFMIN* is the amount of plastic strain before fracture [38,39].

The pressure-compaction relation of the material can be separated into three phases:

- The first phase is linear elastic [39]:

$$P = \frac{P_{\text{crush}}}{\mu_{\text{crush}}}\mu_v \tag{6}$$

where μ_v is the volumetric strain, P_{crush} and μ_{crush} are the crushing pressure and the corresponding volumetric strain.

- The second phase corresponds to the transitional region [39]:

$$P = P_{\text{crush}} + \frac{P_{\text{lock}} - P_{\text{crush}}}{\mu_{\text{lock}} - \mu_{\text{crush}}}(\mu_v - \mu_{\text{crush}}) \tag{7}$$

where P_{lock} and μ_{lock} are the compaction limit and the locking volumetric strain, respectively.

- The third phase describes the response of the fully densified material [39]:

$$P = K_1\bar{\mu} + K_2\bar{\mu}^2 + K_3\bar{\mu}^3 \tag{8}$$

$$\bar{\mu} = \frac{\mu_v - \mu_{lock}}{1 + \mu_{lock}} \tag{9}$$

where K_1, K_2 and K_3 are material parameters, $\bar{\mu}$is the modified volumetric strain.

The input parameters for the HJC model are listed in Table 5. The density ρ, uniaxial compressive strength f_c and the maximum tensile pressure T of the U8*a*1*s* and U16*a*1*s* mixtures are obtained from the experimental results in Section 2. The density and compressive strength of the plain UHPC U8*a* are used for the layer interfacial element. The tensile strength of the interface is assumed to be equal to the bond strength between the U8*a*1*s* and U16*a*1*s* layers, as measured by experiments in Section 2. The input shear modulus in Table 5 is determined by $G = E/2(1 + v)$ with E the Young's modulus and v the Poisson's ratio.

The strength parameters A_c, B_c, N_c, *SFMAX* can be determined by triaxial compressive tests [39]. The test data in the literature [40–43] concerning concrete from 92 MPa to 171 MPa is given in Fig. 7, in which the normalized equivalent stress is $\sigma^* = (\sigma_1 - \sigma_3)/f_c$ and the normalized pressure is $P^* = (\sigma_1 + 2\sigma_3)/3f_c$ [39] (σ_1 and σ_3 are the major and minor principal stresses, respectively). As presented in the figure, the different concrete strength does not cause significant deviations on the relation between σ^* and P^*. Therefore, it is assumed that the developed UHPFRC in this study also possesses a similar trend as that shown in Fig. 7. At a static strain rate $\dot{\varepsilon} = 1.0\ s^{-1}$ and without considering the damage, Eq. (1) with $A_c = 0.79$, $B_c = 1.6$, $N_c = 0.61$ and *SFMAX* = 7 is presented by the solid curve in Fig. 7. These are the default values in the original HJC model [39]. A fair agreement is observed between the experimental data [40–43] and Eq. (1) with the default parameters. That being the case, these values are further used in the HJC model in the present study (see Table 5). Similarly, the strain rate parameter C_c, *EPS*0, and the damage parameters D_1, D_2, *EFMIN* also remain the same as the default values in the original HJC model [39]. These values are widely used for concrete with strengths from 12 MPa to 200 MPa [22,39,44,45], and the strength of the UHPFRC developed in this study also falls within this range.

As regards to the equation of state (EOS) parameters, for the layer interface and the U8*a*1*s* mixture, the crushing pressure P_{crush} and the corresponding volumetric strain μ_{crush} are determined by $P_{\text{crush}} = \sigma_{c,s}/3$ and $\mu_{\text{crush}} = P_{\text{crush}}/K$, in which the bulk modulus $K = E/3(1\text{-}2v)$ [39]. On the other side, for the U16*a*1*s* mixture, the crushing limit and the stiffness of the material are manually enhanced to represent the influences of the larger aggregates. The contributions of the coarse aggregates on improving the ballistic resistance of concrete can be mainly attributed to the following reasons [46]: (1) The stronger coarse aggregates can act as barriers to cracking, as the cracks are driven to cut through the aggregates due to the high stress rate in the case of penetration. (2) The higher hardness of the coarse aggregate increases the kinetic energy loss of the projectile. (3) The direction of the projectile may be changed after it hits the coarse aggregate, which further promotes the energy consumption of the projectile. In the macroscale simulation with symmetric boundary conditions applied to the projectile, the trajectory of the projectile has no deviation, i.e. the direction of the projectile always remains perpendicular to the impact surface of the target. Although the third effect of the coarse aggregates, i.e. due to material heterogeneousness, cannot be reflected in the macroscale model, it is still possible to represent the first two effects of the coarse aggregates, i.e. the improved strength and the enhanced hardness provided by the coarse aggregates. These two effects can be reflected in the macro model by increasing the crushing limit and the stiffness of the material. As given in the HJC model, P_{crush} and μ_{crush} are the thresholds beyond which the voids in the concrete material are gradually compressed [39]. An enhancing factor of 2.5 is applied to the P_{crush} of U16*a*1*s*, which is calibrated by the DOP of the U16*a*1*s* target from the ballistic tests in Section 2 (see Fig. 8). Since the crushing volumetric strain

Table 5
HJC model inputs in LS-DYNA for the simulated UHPFRCs.

Parameters	UHPFRC		Layer interface
	U8*a*1*s*	U16*a*1*s*	
Density ρ (kg/m^3)	2540	2550	2540
Shear modulus G (GPa)	22.5	24.5	25.0
Normalized cohesive strength A_c	0.79	0.79	0.79
Normalized pressure hardening B_c	1.6	1.6	1.6
Strain rate coefficient C_c	0.007	0.007	0.007
Pressure hardening exponent N_c	0.61	0.61	0.61
Uniaxial compressive strength f_c (MPa)	154.9	161.3	149.6
Maximum tensile pressure T (MPa)	12.3	14.6	7.0
Reference stain rate *EPS*0	1.0	1.0	1.0
Plastic strain before fracture *EFMIN*	0.01	0.01	0.01
Normalized maximum strength *SFMAX*	7.0	7.0	7.0
Crushing pressure P_{crush} (MPa)	51.6	134.4	49.9
Crushing volumetric strain μ_{crush}	0.00172	0.00165	0.001497
Locking pressure P_{lock} (GPa)	1.0	1.0	1.0
Locking volumetric strain μ_{lock}	0.1	0.1	0.1
Damage constant D_1	0.04	0.04	0.04
Damage constant D_2	1.0	1.0	1.0
Pressure constant K_1 (GPa)	85	85	850
Pressure constant K_2 (GPa)	−171	−171	−1710
Pressure constant K_3 (GPa)	208	208	2080

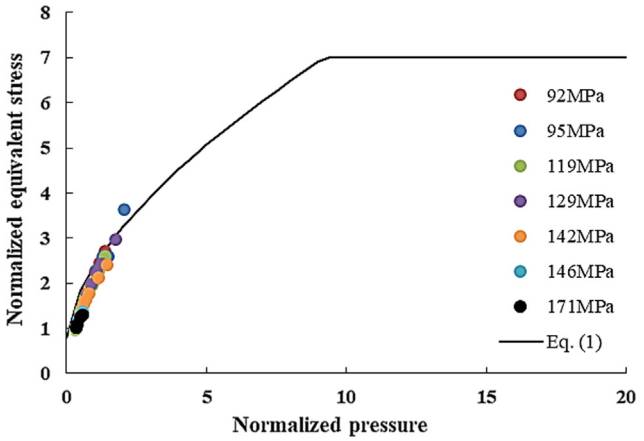

Fig. 7. Determination of strength parameters.

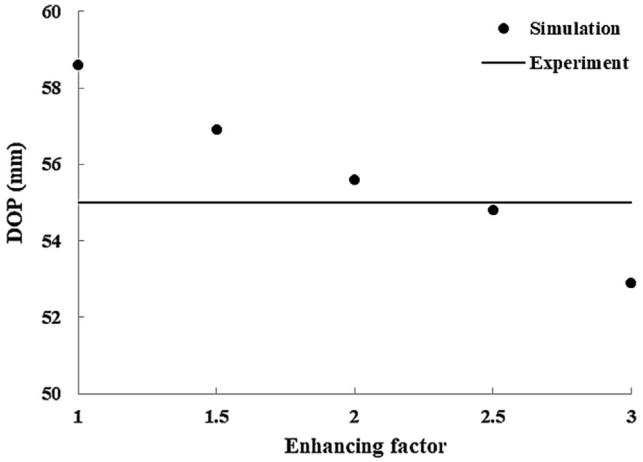

Fig. 8. Calibration of enhancing factor.

μ_{crush} is not changed in the simulation, this enhancing factor improves both the crushing pressure and the stiffness, corresponding to the improved strength and the enhanced hardness of U16*a*1*s*.

Furthermore, the erosion algorithm *MAT_ADD_EROSION is applied to remove the elements with large distortions during the penetration process. The maximum principal strain ε_{max} of 0.5 and the failure volumetric strain ε_{vol} of 0.01 are adopted as the erosion criteria, i.e. the element will be removed if ε_{max} or ε_{vol} reaches the corresponding critical values. These erosion criteria of ε_{max} and ε_{vol} are determined by preliminary study to fit the experimental DOP and D_{eq} of U8*a*1*s*. And they are further used for the other targets, which also show good agreements. Additionally, it is noteworthy that the steel fibers are mainly to increase the tensile strength of the UHPFRC and to decrease the damage scale of the target. Therefore, the influences of fiber addition can be reflected in the model by the maximum tensile pressure T and the above erosion criteria, viz. ε_{max} and ε_{vol} (the crater size D_{eq} is related with these parameters).

4. Model validation and penetration analysis

4.1. Model validation

The DOP obtained by the numerical simulations and the experiments are compared in Table 6 to validate the model. As shown in the table, the simulation results coincide very well with the experimental data, i.e. the deviations are less than 0.5% for both the single- and triple-layered UHPFRC targets. Furthermore, the penetration reductions caused by the 16 mm coarse aggregates and the layered-structure are also successfully captured by the model, showing the reliability of the HJC material model and the corresponding inputs.

The effective strain distribution in the impact surface of the UHPFRC is utilized to denote the crater damage, and the comparisons between the experimental and the numerical D_{eq} are shown in Fig. 9. In general, the numerical simulations are able to reproduce the major damage distribution in the targets, i.e. the difference between the numerical and experimental D_{eq} is less than 5%. Additionally, the comparison between Fig. 9a and 9b indicates that the reduced D_{eq} in the UHPFRC containing larger aggregates, as observed in the experiments, is also successfully shown in the simulations. As demonstrated in Fig. 9, D_{eq} of U16*a*1*s*(90) and its destruction level (represented by the color fringe) are more moderate compared to those of U8*a*1*s*(90), which are in line with the experimental results. In summary, considering both DOP and D_{eq}, fair agreements are achieved by the numerical model and it is hence utilized for the further analysis.

Table 6
Comparisons of DOP.

UHPFRC targets	V_0 (m/s)	DOP (mm)		Error (%)
		Experiment	Simulation	
U8*a*1*s* (90)	841.9	60.0	60.2	0.3
U16*a*1*s* (90)	840.7	55.0	54.8	−0.4
U16*a*1*s*(30)-8*a*1*s*(30)-16*a*1*s*(30)	839.3	52.5	52.6	0.2

4.2. Penetration analysis

4.2.1. Ballistic history

Fig. 10 shows the displacement and velocity histories of the projectiles during the penetration process. The projectiles in U8*a*1*s*(90), U16*a*1*s*(90) and U16*a*1*s*(30)-8*a*1*s*(30)-16*a*1*s*(30) have comparable displacements at the early penetration stage (0–40 μs after impact) because of their similar initial velocities around 840 m/s. However, with the development of the penetration process, the effects of the three targets on the projectile become increasingly obvious. Among the three targets, U16*a*1*s*(30)-8*a*1*s*(30)-16*a*1*s*(30) most effectively reduces the projectile velocity, leading to the smallest projectile displacement in the target, i.e. the simulated DOP. Moreover, the declining rate of the projectile velocity is influenced by the layer interface in U16*a*1*s*(30)-8*a*1*s*(30)-16*a*1*s*(30). Differing with the straight velocity curves of the single-layered targets, the velocity curve of the triple-layered UHPFRC starts to bend when the projectile reaches the layer interface at around 42 μs after impact. This may be attributed to the fact that the layer interface influences the wave propagation and reflection between the layers, affecting the force on the projectile and therefore its velocity. As with the single-layered UHPFRC, the projectile in U16*a*1*s*(90) yields a smaller velocity compared to that in U8*a*1*s*(90) at the same penetrating moment. The DOP in the U16*a*1*s*(90) target is, consequently, smaller.

4.2.2. Penetration process

The penetration processes in the UHPFRC targets are presented by the pressure development in Figs. 11 and 12. U16*a*1*s*(90) is taken as examples of the single-layered UHPFRC target. Pressure is invoked in the target at the moment the projectile reaches the impacted surface. With the further penetrating of the projectile, the pressure develops inwards and it is localized in a region surrounding the head of the projectile (e.g. the pressure distribution at 35 μs). The contact area between the concrete and the projectile experiences the highest pressure, as shown by the red fringe level in the figures. The pressure decreases gradually outwards in the spherical region (presented by the green fringe level), and the remote area in the target is not significantly influenced (indicated by the dark blue fringe level in the figures). The elements near the impacted surface are removed with the projectile penetrating inwards the UHPFRC, forming the impact crater in the target. The velocity of the projectile becomes very small after 100 μs and the pressure distribution around the projectile remains almost unchanged. The velocity of the projectile finally drops to zero at approximately 135 μs.

Furthermore, the simulation of the triple-layered UHPFRC shows that the pressure distribution is affected by the layer interface when the stress wave reaches it, as can be observed by comparing the light blue fringe level in Fig. 11b and Fig. 12b. Furthermore, when the projectile leaves the first layer and enters the second one, e.g. at 63 μs (Fig. 12d), the pressure distribution

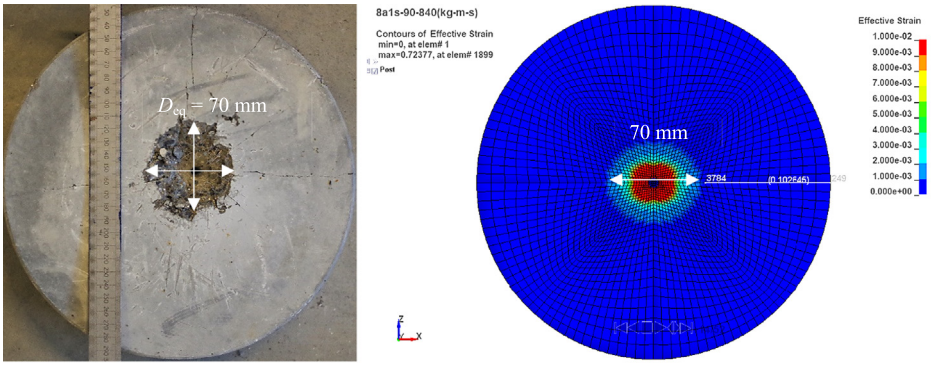

(a) U8*a*1*s*(90)

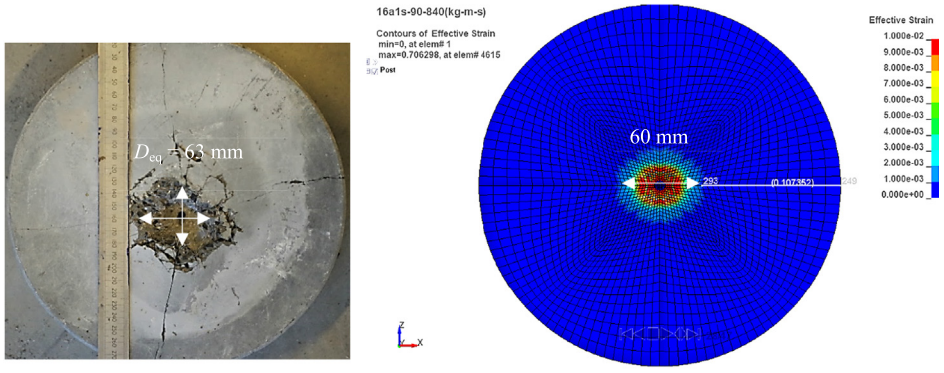

(b) U16*a*1*s*(90)

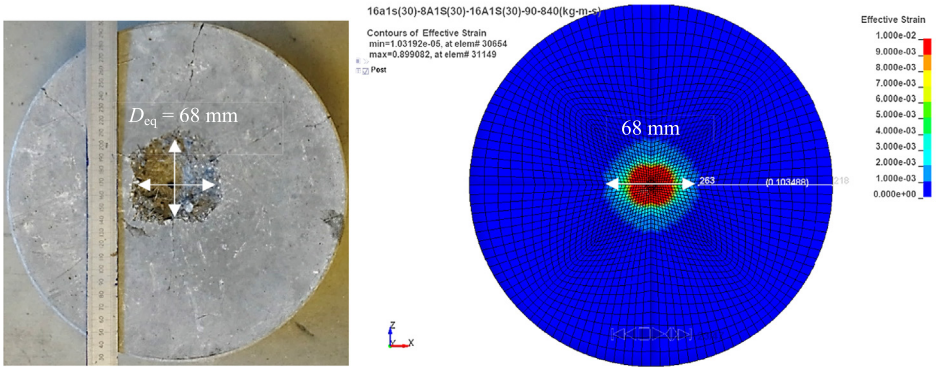

(c) U16*a*1*s*(30)-8*a*1*s*(30)-16*a*1*s*(30)

Fig. 9. Comparisons of $D_{eq.}$

varies. The distinct pressure distribution in the figure also explains the bending velocity curve of the triple-layered UHPFRC target in Fig. 10b. As exhibited in Fig. 12d, the influenced region is divided into two spheres by the layer interface. This may be attributed to the complicated propagation and reflection of the stress wave near the interface, the distinct pressure bearing capacities of the interface and the layer matrix, as well as the different confinement levels of the two layers. Moreover, the existence of the layer interface in the triple-layered UHPFRC dampen the strength of the impact waves [47], which contributes to the smaller DOP and D_{eq} of the target. In addition, the affected area in the triple-layered target is larger than that in the singe-layered counterpart (see the light blue area in Figs. 11 and 12), indicating a higher energy dissipation in U16*a*1*s*(30)-8*a*1*s*(30)-16*a*1*s*(30). This, therefore, further promotes the enhanced impact resistance of the triple-layered UHPFRC.

5. Discussion

5.1. Influences of layer thickness on DOP

Using the validated models, the influences of the target thickness on DOP are discussed. As suggested by the experimental and the simulation results, DOP of U8*a*1*s*(90), U16*a*1*s*(90) and U16*a*1*s*(30)-8*a*1*s*(30)-16*a*1*s*(30) are less than 60 mm, indicating that the 90 mm targets are sufficient to resist the 7.62 mm projectile at around 840 m/s. To achieve a more efficient utilization of the targets, their thicknesses can be reduced. Fig. 13 demonstrates the DOP of the targets with their thickness decreasing from 90 mm to 60 mm. U8*a*1*s* and U16*a*1*s* correspond to the series of the single-layered UHPFRC targets containing the maximum aggregates of 8 mm and 16 mm, respectively (note that their thicknesses are changing). U16*a*1*s*-8*a*1*s*-16*a*1*s* represents the series of the triple-

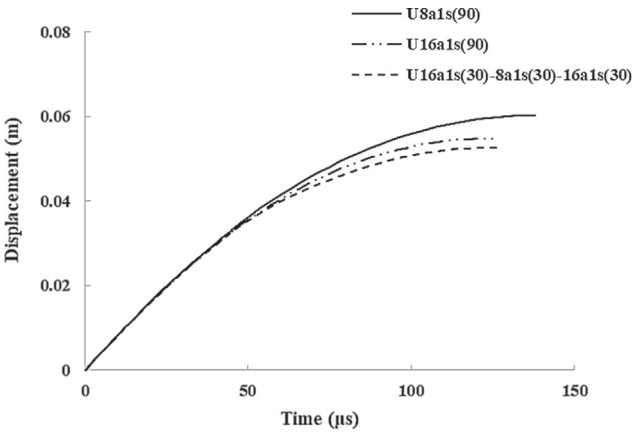

(a) Displacement history

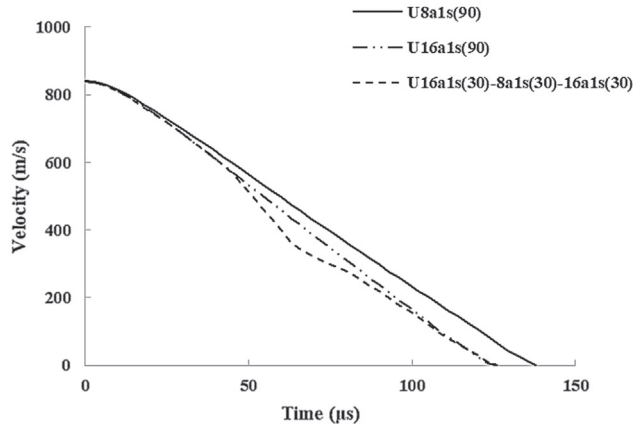

(b) Velocity history

Fig. 10. Penetration history of the projectile.

layered UHPFRC with an equal layer thickness, e.g. when the total thickness of an U16*a*1*s*-8*a*1*s*-16*a*1*s* target is 60 mm, the individual layer thickness is 20 mm. It is noteworthy that the penetration depth in the U16*a*1*s* target with a thickness of 60 mm is around 60.2 mm. In other words, the tip of the projectile slightly crosses the rear surface of the target, as shown in Fig. 14.

Fig. 13 illustrates that the DOP decreases with the increase of the target thickness, nonetheless, the decrease becomes insignificant after the target thickness reaches a critical value. To be more specific, an U8*a*1*s* target with a thickness of 60 mm is totally perforated by the projectile, hence no point corresponding to this case is shown in Fig. 13. However, increasing its thickness from 60 mm to 67.5 mm improves the ballistic resistance remarkably, i.e. the projectile is stopped inside the 67.5 mm target with a DOP of 63.1 mm. The failure pattern of this target is shown in Fig. 15a, in which a major crack appears on the rear surface of the target because of the reflected tensile wave. Further increasing its thickness to 75 mm results in a 2.6 mm reduction in DOP, whereas the reduction becomes insignificant when the target thickness further increases to 82.5 mm and 90 mm. Nevertheless, the rear surface cracking is effectively prevented in these targets thanks to their sufficient thicknesses (see the failure pattern of the 82.5 mm target in Fig. 15b). Similar tendencies can be obtained in the U16*a*1*s* and U16*a*1*s*-8*a*1*s*-16*a*1*s* targets. Moreover, the critical target thickness differs for the three target series: it is around 75 mm for the U8*a*1*s* series, while for U16*a*1*s* the value is around 67.5 mm; as with the triple-layered target, the critical target thickness is smaller than 60 mm.

The reduction of DOP by increasing the target thickness can be attributed to the higher confinement on the projectile provided by the thicker concrete [9]. The larger thickness can generate a more prominent confinement on the inner part of the target, enhancing the energy absorption capacity of the inner concrete [48] and reducing the damage level of the target [9]. Furthermore, the amplitude of the impact wave decreases more significantly when it travels a longer distance inside the thicker target. The impact wave transforms into a tensile one when it reaches the rear surface of the target and reflects at this free boundary. Since the impact wave has a smaller amplitude in the thicker target, the reflected tensile wave is also weaker. Consequently, the caused damage, e.g. cracking, on the rear surface of the thicker target is reduced (see Fig. 15). Nevertheless, the contribution of the target thickness become less significant when the critical target thickness is reached. This critical thickness may be related to the necessary travel length to attenuate the impact wave and to reduce its amplitude below a certain value, so that the reflected tensile stress will be too weak to cause cracking on the rear surface of the UHPFRC. Further increasing the target thickness beyond this critical value will have very limited effects since the strength of the tensile wave is already sufficiently small.

Additionally, comparing the DOP of U8*a*1*s* and U16*a*1*s* series in Fig. 13 reveals that the larger coarse aggregates play an important role on improving the ballistic resistance of the UHPFRC, and this influence is more obvious with a smaller target thickness. For instance, the DOP in the 67.5 mm target has an approximate 12% reduction when the maximum aggregate size increases from 8 mm to 16 mm, while the reduction is around 9% when the target thickness is 90 mm. Moreover, Fig. 13 shows that the U16*a*1*s*-8*a*1*s*-16*a*1*s* series has the smallest DOP among the three simulated target series with the same thickness. For example, the DOP in the U8*a*1*s*, U16*a*1*s* and U16*a*1*s*-8*a*1*s*-16*a*1*s* targets with a thickness of 75 mm are about 60.5 mm, 54.8 mm and 52.6 mm, respectively. The lower DOP of the U16*a*1*s*-8*a*1*s*-16*a*1*s* series in the whole thickness range reveals that the triple-layered UHPFRC possesses an enhanced resistance compared to its single-layered counterparts with the same target thickness. This also indicates the possibility of using a thinner triple-layered target instead of a thicker single-layered one to achieve the same level of protection, e.g. the 60 mm U16*a*1*s*-8*a*1*s*-16*a*1*s* target may be used to replace the 90 mm U16*a*1*s* target considering their comparable DOP.

5.2. Influences of penetration velocity on perforation limit

Perforation limit h_e is defined as the minimum target thickness required to prevent perforation [21], and it is an important characterization for ballistic engineers to design safety protective structures. A number of empirical formulae have been developed to predict the perforation limit of concrete material, among which the BRL formula, ACE formula, modified NDRC formula and CEA-EDF formula are extensively utilized. The expressions of these formulae are given as follows [21].

- BRL formula [21]:

$$\frac{h_e}{d} = \frac{1.729 \times 10^{-3}}{\sqrt{\sigma_{c,s}}} \left(\frac{M}{d^3}\right) d^{0.2} V_0^{1.33} \tag{10}$$

- ACE formula [21]:

$$\frac{h_e}{d} = \frac{4.34 \times 10^{-4}}{\sqrt{\sigma_{c,s}}} \left(\frac{M}{d^3}\right) d^{0.215} V_0^{1.5} + 1.94 \tag{11}$$

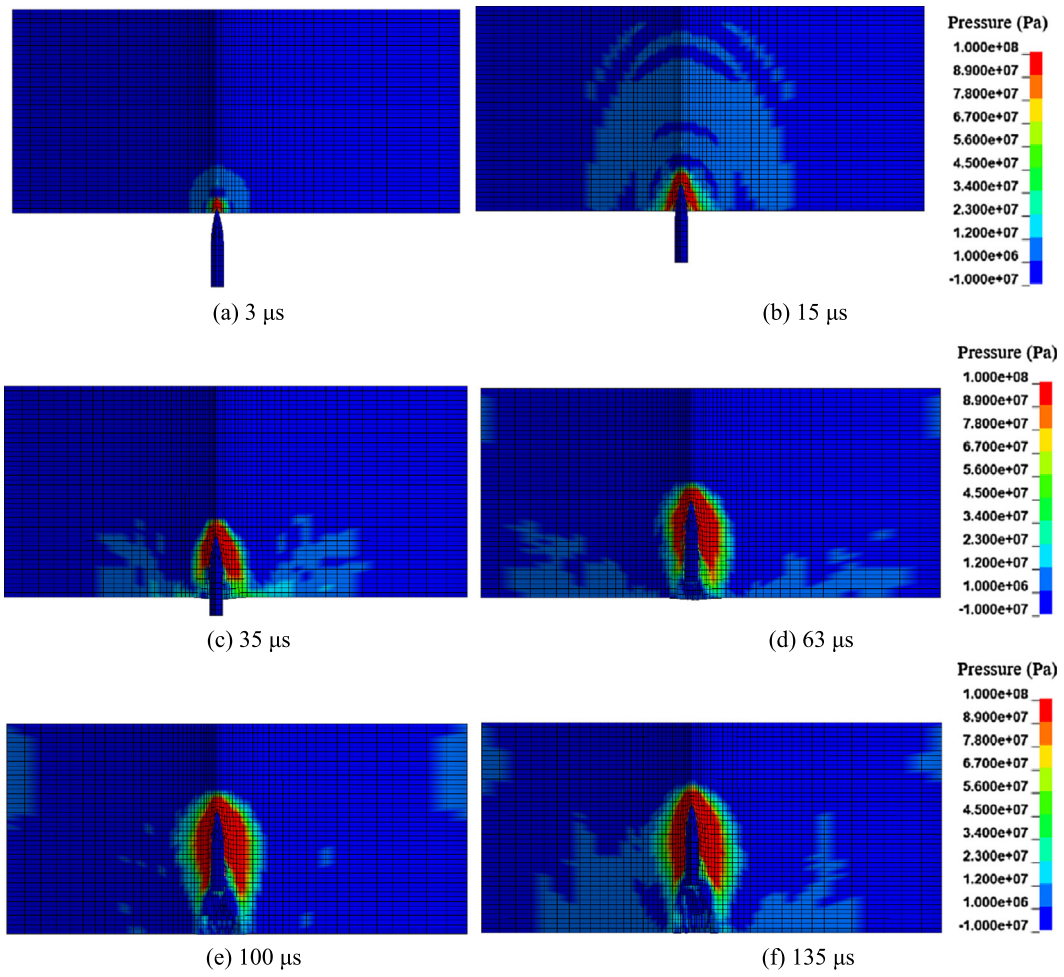

Fig. 11. Pressure development in U16*a*1*s*(90).

- CEA-EDF formula [21]:

$$\frac{h_e}{d} = 0.82\frac{M^{0.5}{V_0}^{0.75}}{\rho^{0.125}{\sigma_{c,s}}^{0.375}d^{1.5}} \tag{12}$$

- Modified NDRC formula [21]:

$$G_n = 3.8\times10^{-5}\frac{N^*M}{d\sqrt{\sigma_{c,s}}}\left(\frac{V_0}{d}\right)^{1.8} \tag{13a}$$

$$\frac{DOP}{d} = 2G_n^{0.5}\ \text{for}\ G_n \geqslant 1 \tag{13b}$$

$$\frac{DOP}{d} = G_n + 1\ \text{for}\ G_n < 1 \tag{13c}$$

$$\frac{h_e}{d} = 3.19\frac{DOP}{d} - 0.718\left(\frac{DOP}{d}\right)^2\ \text{for}\ h_e/d \leqslant 3 \tag{13d}$$

$$\frac{h_e}{d} = 1.32 + 1.24\frac{DOP}{d}\ \text{for}\ 3 < h_e/d < 18 \tag{13e}$$

where N^* is the nose shape factor, N^* = 0.72, 0.84, 1.0 and 1.14 for flat, blunt, spherical and sharp heads, respectively.

The h_e of the U8*a*1*s*, U16*a*1*s* and U16*a*1*s*-8*a*1*s*-16*a*1*s* target series under impact velocities from 640 m/s to 940 m/s are approximately estimated by the numerical models. The results are illustrated in Table 7 together with the calculated h_e by the above empirical formulae. Note that for the triple-layered UHPFRC, equivalent concrete properties obtained according to the composite theory [49] are used as the input parameters for the empirical formulae. For instance, the equivalent compressive strength of the triple-layered UHPFRC $\sigma_{c,eq}$ used in the empirical formulae is the arithmetic mean of the layers' compressive strength:

$$\sigma_{c,eq} = (\sigma_{c,s,1}H_1 + \sigma_{c,s,2}H_2 + \sigma_{c,s,3}H_3)/(H_1 + H_2 + H_3) \tag{14}$$

where $\sigma_{c,s,i}$ and H_i are the compressive strength and thickness of the i^{th} layer, i = 1, 2, 3.

As shown in Table 7, the ACE formula gives results that are closest to the numerical h_e of the U8*a*1*s* series at the whole velocity range, and predictions for the U16*a*1*s* series at high velocities namely 840 m/s and 940 m/s are also acceptable. The modified NDRC formula yields results comparable to the numerical h_e of U16*a*1*s* at 640 m/s and 740 m/s, as well as those of U16*a*1*s*-8*a*1*s*-16*a*1*s* at 640 m/s, 740 m/s and 840 m/s. In contrast, the numerical h_e of U16*a*1*s*-8*a*1*s*-16*a*1*s* at 940 m/s falls between the estimations of the modified NDRC and ACE formulae. Accordingly, none of these existing empirical formulae is able to predict the h_e of the developed UHPFRC from 640 m/s to 940 m/s. This is because these formulae are proposed based on the regression analyses of certain types of concrete under certain impact velocities, which limits

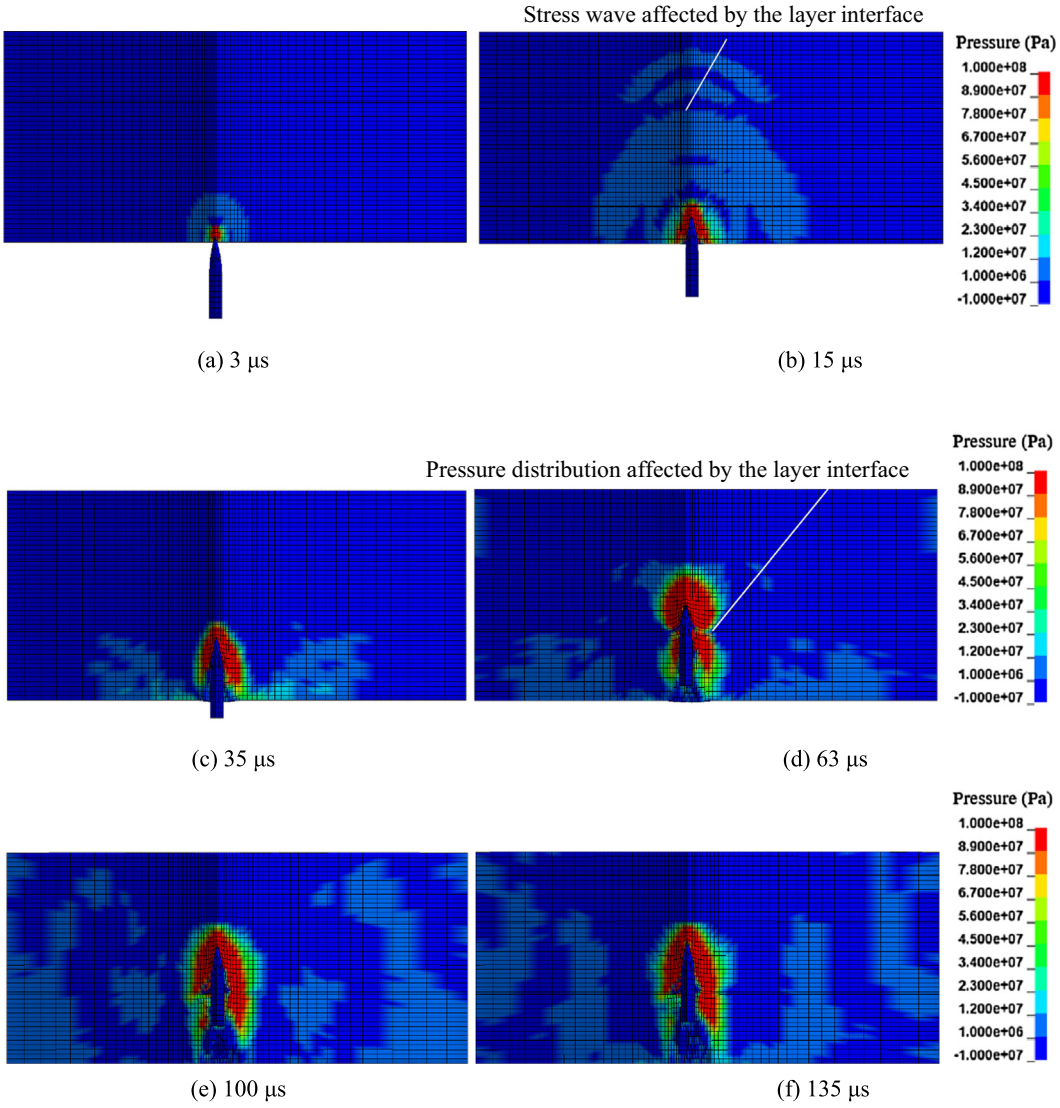

Fig. 12. Pressure development in U16*a*1*s*(30)-8*a*1*s*(30)-16*a*1*s*(30).

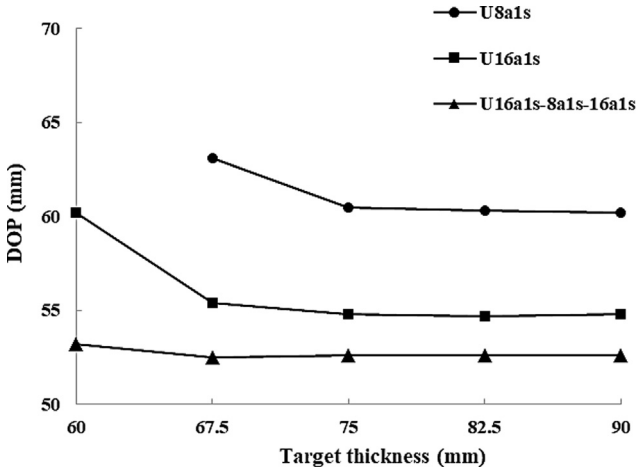

Fig. 13. Influence of target thickness.

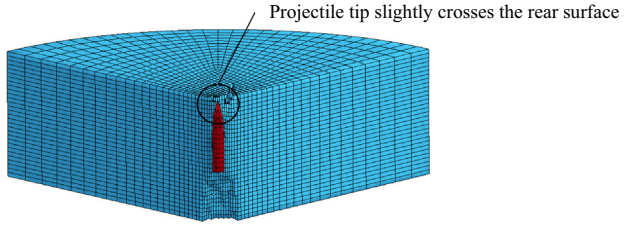

Fig. 14. Failure pattern of U16*a*1*s* target with a thickness of 60 mm.

their application ranges [50]. Since UHPFRC is a relatively new material, these empirical formulae are not exactly proposed for it and their validity has not been verified against impacts of UHPFRC, not to mention the coarse-aggregated layered UHPFRC. That being the case, the ACE formula is modified to give more accurate predictions for the coarse-aggregated layered UHPFRC developed in this study. The modified ACE formulae are obtained on the basis of the simulation results in Table 7, and the expressions are given below:

$$\frac{h_e}{d} = \frac{4.34\times10^{-4}}{\sqrt{\sigma_{c,s}}}\left(\frac{M}{d^3}\right)d^{0.215}V_0^{1.5} + 1.73 \text{ for U8a1}s \tag{15a}$$

$$\frac{h_e}{d} = \frac{4.34\times10^{-4}}{\sqrt{\sigma_{c,s}}}\left(\frac{M}{d^3}\right)d^{0.215}V_0^{1.5} + 1.42 \text{ for U16a1}s \tag{15b}$$

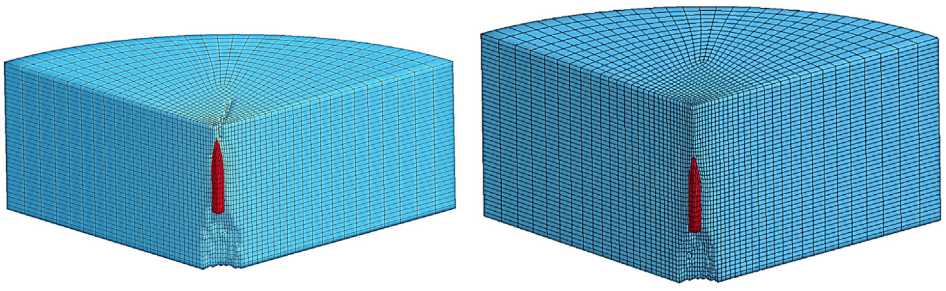

(a) 67.5 mm (b) 82.5 mm

Fig. 15. Failure pattern of U8*a*1*s* targets with different thickness.

Table 7
Perforation limits at different velocities following the simulation and empirical formulae.

V_0 (m/s)	Method	h_e (mm)		
		U8*a*1*s*	U16*a*1*s*	U16*a*1*s*-8*a*1*s*-16*a*1*s*
640	Simulation	48.0	45.0	42.0
	BRL	51.1	50.1	50.4
	ACE	50.6	49.8	50.1
	CEA-EDF	39.1	38.5	38.7
	Modified NDRC	45.4	45.1	45.2
740	Simulation	57.0	54.0	48.0
	BRL	62.0	60.8	61.2
	ACE	59.3	58.4	58.7
	CEA-EDF	43.6	42.9	43.1
	Modified NDRC	50.4	50.0	50.1
840	Simulation	67.5	63.0	57.0
	BRL	73.4	71.9	72.4
	ACE	68.6	67.5	67.9
	CEA-EDF	47.9	47.2	47.4
	Modified NDRC	55.2	54.8	54.9
940	Simulation	78.0	75.0	67.5
	BRL	82.3	83.5	84.1
	ACE	78.5	77.2	77.6
	CEA-EDF	52.2	51.4	51.6
	Modified NDRC	60.1	59.5	59.7

$$\frac{h_e}{d} = \frac{4.34 \times 10^{-4}}{\sqrt{\sigma_{c,s}}} \left(\frac{M}{d^3}\right) d^{0.215} V_0^{1.5} + 0.63 \text{ for U16}a1s - 8a1s - 16a1s \tag{15c}$$

The comparisons between the h_e from the numerical simulation and the modified ACE formulae are shown in Fig. 16. Excellent agreements are observed. It is worth mentioning that similar to the existing empirical formulae, the modified ACE formulae have also their applied range. They are proposed for the coarse-aggregated layered UHPFRC against the 7.62 mm projectile under impact velocities between 640 m/s and 940 m/s. Using them for larger-caliber projectile may lead to underestimation of the DOP due to the scaling effect, which can be attributed to the inconsistent size variations of the projectile and the aggregates [51].

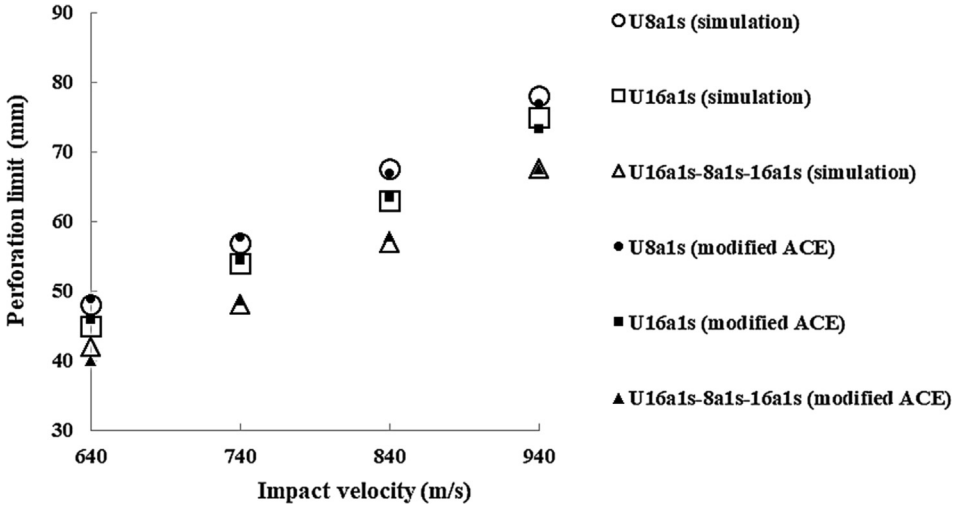

Fig. 16. Comparison between simulation and modified ACE formulae.

Table 8
Cement amount to cast one UHPFRC target with a diameter of 275 mm and a thickness of h_e.

Initial velocity V_0 (m/s)	Material amounts (kg)					
	U8*a*1*s*		U16*a*1*s*		U16*a*1*s*-8*a*1*s*-16*a*1*s*	
	cement	fiber	cement	fiber	cement	fiber
640	1.68	0.22	1.40	0.21	1.36	0.20
740	1.99	0.27	1.68	0.25	1.56	0.22
840	2.36	0.31	1.96	0.29	1.85	0.27
940	2.72	0.36	2.34	0.35	2.19	0.31

Furthermore, as depicted by the numerical results in Table 7, h_e increases with the increase of V_0; and the U8*a*1*s* series has the largest h_e, while U16*a*1*s*-8*a*1*s*-16*a*1*s* the smallest value. For example, the simulation exhibits that for an U8*a*1*s* target, the smallest thicknesses to prevent perforation under 640 m/s and 940 m/s are about 48 mm and 78 mm, respectively. On the contrary, those corresponding to the U16*a*1*s*-8*a*1*s*-16*a*1*s* series are only 42 mm and 67.5 mm, decreasing 14% and 16%, respectively, compared to those of U8*a*1*s*.

The smaller h_e of the U16*a*1*s*-8*a*1*s*-16*a*1*s* series indicates the feasibility to reduce the target thickness by applying the layered-structure, which then results in the reductions of the required materials, e.g. cement and steel fibers. Table 8 gives the cement and fiber amounts to cast a UHPFRC target with a diameter of 275 mm and a thickness of h_e (obtained from the simulations in Table 7). Thanks to the enhanced impact resistance of the triple-layered UHPFRC, the cement and fiber amounts required to cast the U16*a*1*s*-8*a*1*s*-16*a*1*s* targets are obviously reduced compared with their single-layered counterparts. To be more precise, the cement amounts for the U16*a*1*s*-8*a*1*s*-16*a*1*s* targets under 640 m/s, 740 m/s 840 m/s and 940 m/s are about 19%, 22%, 22% and 20% less than those for the U8*a*1*s* targets; and the corresponding fiber amount reductions are 13%, 16%, 16% and 13%, respectively. As a consequence, with the same level of ballistic resistance, the triple-layered UHPFRC consumes less materials than the single-layered one, making the layered target more sustainable and more economic. In addition, the lighter weight of the triple-layered UHPFRC target is also beneficial for its transportation and installation.

6. Conclusions

This study numerically investigates the ballistic performance of the coarse-aggregated layered UHPFRC with LS-DYNA. Mechanical and ballistic experiments are conducted to provide model inputs and to validate the simulations. After model validation, the displacement and velocity histories of the projectile, as well as the dynamic penetration process in the UHPFRC targets are analyzed. Furthermore, the effects of the target thickness on the DOP, and the influences of the impact velocity on the perforation limit h_e are discussed. In addition, modified ACE formulae to accurately predict the h_e of the coarse-aggregated layered UHPFRC are proposed based on the simulations. The study promotes a better understanding of ballistic responses of the coarse-aggregated layered UHPFRC. The following conclusions can be drawn:

(1) The numerical simulations of the U8*a*1*s*(90), U16*a*1*s*(90) and U16*a*1*s*(30)-8*a*1*s*(30)-16*a*1*s*(30) targets coincide well with the experimental results. The difference between of the DOP and the crater size obtained by the experiments and the simulations are smaller than 0.5% and 5%, respectively.
(2) The HJC constitutive model in LS-DYNA can well characterize the dynamic response of the coarse-aggregated UHPFRC subjected to projectile impacts; and the improved ballistic resistance provided by the coarse aggregates can be reflected by increasing the crushing pressure in the model.
(3) The layer interface affects the pressure distribution in the triple-layered target and thus the velocity history of the projectile. This can be attributed to the complicated propagation and reflection of the stress wave near the interface, the distinct pressure bearing capacities of the interface and the layer matrix, as well as the different confinement levels of the two layers.
(4) The DOP decreases with the increase of the target thickness; however, the reduction becomes very limited when the critical target thickness is reached. The critical thickness is around 75 mm, 67.5 mm and 60 mm for the U8*a*1*s*, U16*a*1*s* and U16*a*1*s*-8*a*1*s*-16*a*1*s* targets, respectively.
(5) The h_e increases with the increase of the penetration velocity. Under the same velocity, U8*a*1*s* has the largest h_e while U16*a*1*s*-8*a*1*s*-16*a*1*s* achieves the smallest value, indicating the feasibility to produce thinner target with the layered structure concept. Consequently, the triple-layered UHPFRC consumes fewer dosages of cement and fibers than the single-layered one with the same level of protection, making the layered target more environmentally and economically attractive.

CRediT authorship contribution statement

Y.Y.Y. Cao: Methodology, Investigation, Software, Data curation, Formal analysis, Validation, Writing - original draft. **Qingliang Yu:** Conceptualization, Supervision, Project administration, Writing - review & editing. **W.H. Tang:** Writing - review & editing. **H.J.H. Brouwers:** Supervision, Writing - review & editing.

Declaration of Competing Interest

The authors declare that they have no known competing financial interests or personal relationships that could have appeared to influence the work reported in this paper.

Acknowledgment

This research was carried out under the funding and support of China Scholarship Council and Eindhoven University of Technology.

References

[1] Y.Y.Y. Cao, Q.L. Yu, H.J.H. Brouwers, W. Chen, Predicting the rate effects on hooked-end fiber pullout performance from Ultra- High Performance Concrete, Cem. Concr. Res. (2019), https://doi.org/10.1182/blood-2016-03-705590.
[2] Z. Wu, C. Shi, W. He, D. Wang, Static and dynamic compressive properties of ultra-high performance concrete (UHPC) with hybrid steel fiber reinforcements, Cem. Concr. Compos. 79 (2017) 148–157, https://doi.org/10.1016/j.cemconcomp.2017.02.010.
[3] Q. Song, R. Yu, Z. Shui, S. Rao, X. Wang, M. Sun, C. Jiang, Steel fibre content and interconnection induced electrochemical corrosion of Ultra-High Performance

Fibre Reinforced Concrete (UHPFRC), Cem. Concr. Compos. 94 (2018) 191–200, https://doi.org/10.1016/j.cemconcomp.2018.09.010.
[4] P. Máca, R. Sovják, P. Konvalinka, Mix design of UHPFRC and its response to projectile impact, Int. J. Impact Eng. 63 (2014) 158–163, https://doi.org/10.1016/j.ijimpeng.2013.08.003.
[5] J. Liu, C. Wu, Y. Su, J. Li, R. Shao, G. Chen, Z. Liu, Experimental and numerical studies of ultra-high performance concrete targets against high-velocity projectile impacts, Eng. Struct. 173 (2018) 166–179, https://doi.org/10.1016/j.engstruct.2018.06.098.
[6] R. Yu, P. Spiesz, H.J.H. Brouwers, Energy absorption capacity of a sustainable Ultra-High Performance Fibre Reinforced Concrete (UHPFRC) in quasi-static mode and under high velocity projectile impact, Cem. Concr. Compos. 68 (2016) 109–122, https://doi.org/10.1016/j.cemconcomp.2016.02.012.
[7] X. Wang, R. Yu, Q. Song, Z. Shui, Z. Liu, S. Wu, D. Hou, Optimized design of ultra-high performance concrete (UHPC) with a high wet packing density, Cem. Concr. Res. 126 (2019), https://doi.org/10.1016/j.cemconres.2019.105921 105921.
[8] C. Shi, Z. Wu, J. Xiao, D. Wang, Z. Huang, Z. Fang, A review on ultra high performance concrete: part I. Raw materials and mixture design, Constr. Build. Mater. 101 (2015) 741–751, https://doi.org/10.1016/j.conbuildmat.2015.10.088.
[9] P.P. Li, H.J.H. Brouwers, Q. Yu, Influence of key design parameters of ultra-high performance fibre reinforced concrete on in-service bullet resistance, Int. J. Impact Eng. 136 (2020), https://doi.org/10.1016/j.ijimpeng.2019.103434.
[10] A.N. Dancygier, High-performance concrete engineered for protective barriers, Philos. Trans. R. Soc. A Math. Phys. Eng. Sci. 375 (2017), https://doi.org/10.1098/rsta.2016.0180.
[11] M.H. Zhang, M.S.H. Sharif, G. Lu, Impact resistance of high-strength fibre-reinforced concrete, Mag. Concr. Res. 59 (2007) 199–210, https://doi.org/10.1680/macr.2007.59.3.199.
[12] Y. Peng, H. Wu, Q. Fang, J.Z. Liu, Z.M. Gong, Impact resistance of basalt aggregated UHP-SFRC/fabric composite panel against small caliber arm, Int. J. Impact Eng. 88 (2016) 201–213, https://doi.org/10.1016/j.ijimpeng.2015.10.011.
[13] Y. Peng, H. Wu, Q. Fang, J.Z. Liu, Z.M. Gong, Flat nosed projectile penetrating into UHP-SFRC target: experiment and analysis, Int. J. Impact Eng. 93 (2016) 88–98, https://doi.org/10.1016/j.ijimpeng.2016.02.012.
[14] H. Wu, Q. Fang, J. Gong, J.Z. Liu, J.H. Zhang, Z.M. Gong, Projectile impact resistance of corundum aggregated UHP-SFRC, Int. J. Impact Eng. 84 (2015) 38–53, https://doi.org/10.1016/j.ijimpeng.2015.05.007.
[15] Z. Wu, C. Shi, W. He, Comparative study on flexural properties of ultra-high performance concrete with supplementary cementitious materials under different curing regimes, Constr. Build. Mater. 136 (2017) 307–313, https://doi.org/10.1016/j.conbuildmat.2017.01.052.
[16] Y.Y.Y. Cao, P.P. Li, H.J.H. Brouwers, M. Sluijsmans, Q.L. Yu, Enhancing flexural performance of ultra-high performance concrete by an optimized layered-structure concept, Compos. Part B Eng. 171 (2019) 154–165, https://doi.org/10.1016/j.compositesb.2019.04.021.
[17] S.T. Quek, V.W.J. Lin, M. Maalej, Development of functionally-graded cementitious panel against high-velocity small projectile impact, Int. J. Impact Eng. 37 (2010) 928–941, https://doi.org/10.1016/j.ijimpeng.2010.02.002.
[18] Y.S. Tai, Flat ended projectile penetrating ultra-high strength concrete plate target, Theor. Appl. Fract. Mech. 51 (2009) 117–128, https://doi.org/10.1016/j.tafmec.2009.04.005.
[19] J. Liu, C. Wu, X. Chen, Numerical study of ultra-high performance concrete under non-deformable projectile penetration, Constr. Build. Mater. 135 (2017) 447–458, https://doi.org/10.1016/j.conbuildmat.2016.12.216.
[20] Y.Y.Y. Cao, Q.H. Tan, Z.G. Jiang, H.J.H. Brouwers, Q.L. Yu, A nonlinear rate-dependent model for predicting the depth of penetration in Ultra-High Performance Fiber Reinforced Concrete (UHPFRC), Cem. Concr. Compos. 106 (2020), https://doi.org/10.1016/j.cemconcomp.2019.103451 103451.
[21] Q.M. Li, S.R. Reid, H.M. Wen, A.R. Telford, Local impact effects of hard missiles on concrete targets, Int. J. Impact Eng. 32 (2006) 224–284, https://doi.org/10.1016/j.ijimpeng.2005.04.005.
[22] Y. Peng, H. Wu, Q. Fang, Z.M. Gong, Geometrical scaling effect for penetration depth of hard projectiles into concrete targets, Int. J. Impact Eng. 120 (2018) 46–59, https://doi.org/10.1016/j.ijimpeng.2018.05.010.
[23] R. Yu, Development of sustainable protective Ultra-High Performance Fibre Reinforced Concrete (UHPFRC), Eindhoven University of Technology, 2015.
[24] R. Sovják, T. Vavřiník, J. Zatloukal, P. Máca, T. Mičunek, M. Frydrýn, Resistance of slim UHPFRC targets to projectile impact using in-service bullets, Int. J. Impact Eng. 76 (2015) 166–177, https://doi.org/10.1016/j.ijimpeng.2014.10.002.
[25] H.J.H. Brouwers, H.J. Radix, Self-compacting concrete: theoretical and experimental study, Cem. Concr. Res. 35 (2005) 2116–2136, https://doi.org/10.1016/j.cemconres.2005.06.002.
[26] X. Wang, K. Wang, P. Taylor, G. Morcous, Assessing particle packing based self-consolidating concrete mix design method, Constr. Build. Mater. 70 (2014) 439–452, https://doi.org/10.1016/j.conbuildmat.2014.08.002.
[27] Q.L. Yu, P. Spiesz, H.J.H. Brouwers, Development of cement-based lightweight composites – Part 1: mix design methodology and hardened properties, Cem. Concr. Compos. 44 (2013) 17–29, https://doi.org/10.1016/j.cemconcomp.2013.03.030.
[28] P.P. Li, Q.L. Yu, H.J.H. Brouwers, Effect of coarse basalt aggregates on the properties of Ultra-high Performance Concrete (UHPC), Constr. Build. Mater. 170 (2018) 649–659, https://doi.org/10.1016/j.conbuildmat.2018.03.109.
[29] P.P. Li, Y.Y.Y. Cao, H.J.H. Brouwers, W. Chen, Q.L. Yu, Development and properties evaluation of sustainable ultra-high performance pastes with quaternary blends, J. Clean. Prod. 240 (2019), https://doi.org/10.1016/j.jclepro.2019.118124 118124.
[30] T.H. Almusallam, N.A. Siddiqui, R.A. Iqbal, H. Abbas, Response of hybrid-fiber reinforced concrete slabs to hard projectile impact, Int. J. Impact Eng. 58 (2013) 17–30, https://doi.org/10.1016/j.ijimpeng.2013.02.005.
[31] H. Wu, Q. Fang, X.W. Chen, Z.M. Gong, J.Z. Liu, Projectile penetration of ultra-high performance cement based composites at 510–1320 m/s, Constr. Build. Mater. 74 (2015) 188–200, https://doi.org/10.1016/j.conbuildmat.2014.10.041.
[32] EN 12390–3, Testing hardened concrete - Part 3: Compressive strength of test specimens, 2009.
[33] EN 12390-6, Testing hardened concrete – Part 6: Tensile splitting strength of test specimens, 2000.
[34] Y. Qian, D. Zhang, T. Ueda, Tensile bond between substrate concrete and normal repairing mortar under freeze – thaw cycles, in: 4th Int. Conf. Durab. Concr. Struct., Purdue University, West Lafayette, IN, USA, 2014: pp. 385–392.
[35] J.K. Holmen, J.K. Solberg, O.S. Hopperstad, T. Børvik, Ballistic impact of layered and case-hardened steel plates, Int. J. Impact Eng. 110 (2017) 4–14, https://doi.org/10.1016/j.ijimpeng.2017.02.001.
[36] LSTC, LS-DYNA® Keyword User ' S Manual Volume I, Livermore Software Technology Corporation, 2015.
[37] LSTC, ls-dyna Theory Manual, 2016th ed., Livermore Software Technology Corporation 7374, California, 2016.
[38] LSTC, LS-DYNA® Keyword User ' S Manual Volume II, Livermore Software Technology Corporation, 2015.
[39] G.M. Ren, H. Wu, Q. Fang, X.Z. Kong, Parameters of Holmquist–Johnson–Cook model for high-strength concrete-like materials under projectile impact, Int. J. Prot. Struct. 8 (2017) 352–367, https://doi.org/10.1177/2041419617721552.
[40] G.M. Ren, H. Wu, Q. Fang, J.Z. Liu, Z.M. Gong, Triaxial compressive behavior of UHPCC and applications in the projectile impact analyses, Constr. Build. Mater. 113 (2016) 1–14, https://doi.org/10.1016/j.conbuildmat.2016.02.227.
[41] Y. Farnam, M. Moosavi, M. Shekarchi, S.K. Babanajad, A. Bagherzadeh, Behaviour of Slurry Infiltrated Fibre Concrete (SIFCON) under triaxial compression, Cem. Concr. Res. 40 (2010) 1571–1581, https://doi.org/10.1016/j.cemconres.2010.06.009.
[42] R. Sovják, F. Vogel, B. Beckmann, Triaxial compressive strength of ultra high performance concrete, Acta Polytech. 53 (2013) 901–905, https://doi.org/10.14311/AP.2013.53.0901.
[43] J. Xie, A.E. Elwi, J.G. MacGregor, Mechanical properties of three high-strength concretes containing silica fume, ACI Mater. J. 92 (1995) 135–145.
[44] J. Lai, X. Guo, Y. Zhu, Repeated penetration and different depth explosion of ultra-high performance concrete, Int. J. Impact Eng. 84 (2015) 1–12, https://doi.org/10.1016/j.ijimpeng.2015.05.006.
[45] H. Xu, H.M. Wen, A computational constitutive model for concrete subjected to dynamic loadings, Int. J. Impact Eng. 91 (2016) 116–125, https://doi.org/10.1016/j.ijimpeng.2016.01.003.
[46] S. Wang, H.T.N. Le, L.H. Poh, H. Feng, M.H. Zhang, Resistance of high-performance fiber-reinforced cement composites against high-velocity projectile impact, Int. J. Impact Eng. 95 (2016) 89–104, https://doi.org/10.1016/j.ijimpeng.2016.04.013.
[47] X. Chen, N. Chandra, The effect of heterogeneity on plane wave propagation through layered composites, Compos. Sci. Technol. 64 (2004) 1477–1493, https://doi.org/10.1016/j.compscitech.2003.10.024.
[48] F. Wan, Z. Jiang, Q. Tan, Y. Cao, Response of steel-tube-confined concrete targets to projectile impact, Int. J. Impact Eng. 94 (2016) 50–59, https://doi.org/10.1016/j.ijimpeng.2016.03.012.
[49] B. Xu, H.A. Toutanji, J. Gilbert, Impact resistance of poly(vinyl alcohol) fiber reinforced high-performance organic aggregate cementitious material, Cem. Concr. Res. 40 (2010) 347–351, https://doi.org/10.1016/j.cemconres.2009.09.006.
[50] Q.M. Li, X.W. Chen, Dimensionless formulae for penetration depth of concrete target impacted by a non-deformable projectile, Int. J. Impact Eng. 28 (2003) 93–116, https://doi.org/10.1016/S0734-743X(02)00037-4.
[51] H. Wu, Y.C. Li, Q. Fang, Y. Peng, Scaling effect of rigid projectile penetration into concrete target: 3D mesoscopic analyses, Constr. Build. Mater. 208 (2019) 506–524, https://doi.org/10.1016/j.conbuildmat.2019.03.040.